A 65-nm Sub-10-mW Communication/Ranging Quadrature Uncertain-IF IR-UWB Transceiver With Twin-OOK Modulation

Bowen Wang, *Graduate Student Member, IEEE*, Woogeun Rhee, *Fellow, IEEE*,
and Zhihua Wang, *Fellow, IEEE*

***Abstract*—This article describes a robust noncoherent transceiver architecture for pulse-based ultrawideband (UWB) communication systems. To address synchronization and interference issues in the conventional noncoherent transceiver with on–off keying (OOK) modulation, two techniques are proposed. The first one is twin-OOK (T-OOK) modulation, in which two pulses are used to represent 1-bit data. A short-duration synchronization pulse is employed for baseband synchronization, while a long-duration data pulse based on frequency-hopping (FH) OOK is employed for data transmission. The proposed modulation scheme not only addresses the synchronization problem of a transceiver baseband but also enhances the spectrum efficiency of a transmitter by adopting an FH method. The second one is uncertain-intermediate frequency (IF) down-conversion with quadrature demodulation. The quadrature uncertain-IF receiver achieves robust demodulation over frequency drift and good narrowband-interference (NBI) tolerance with an on-chip bandpass filter (BPF). In addition, ranging accuracy is enhanced with in-phase and quadrature (IQ) two-path signals. A prototype 6–8-GHz communication/ranging UWB transceiver is implemented in 65-nm CMOS. The transceiver achieves–71-dBm sensitivity at 10 Mb/s and 0.96-cm root-mean-square (rms) ranging accuracy. The transmitter and the receiver have the power consumption of 3.83 and 5.38 mW, respectively.**

***Index Terms*—Frequency hopping (FH), low-power wireless connectivity, ranging, transceiver, twin-OOK (T-OOK) modulation, ultrawideband (UWB), uncertain-intermediate frequency (IF).**

I. INTRODUCTION

THE development of low-power wireless connectivity has been accelerating with countless applications in the Internet-of-Things (IoT) and biomedical wearable devices. The conventional narrowband wireless connectivity standards, such as Bluetooth low energy (BLE) and Wi-Fi, do not satisfy the requirements of various applications for flexible data rate, high energy efficiency, and fine ranging accuracy. The BLE transceiver consumes less than 10 mW of power but suffers from a very limited data rate [1], [2], [3], [4], [5], [6]. Even though the new Wi-Fi standards support >1-Gb/s data transmission, system power consumption over 100 mW is unbearable for low-power IoT applications [7], [8], [9]. In addition, due to their inability to provide centimeter-level ranging accuracy, narrowband transceivers are not suitable for fine ranging applications, such as indoor location tracking and secure wireless connectivity.

A revived technique, the ultrawideband (UWB) one, has been recognized as a promising candidate for next-generation wireless connectivity. In the UWB technique, users communicate with each other by transmitting short-duration pulses. The short-duration pulses occupy a wide signal bandwidth in the frequency domain. Having short-duration pulses and wide signal bandwidth, the UWB technique has two major advantages. First, the UWB transceiver can either support high-data-rate communications [10], [11], [12] or improve the system energy efficiency by operating in a duty-cycled manner for low-data-rate applications [13]. Second, the UWB signal offers a high ranging resolution, which is useful for secure short-range communications [14], [15]. Even though the standard-compliant coherent UWB transceiver with high-rate pulses (HRP) can achieve robust transmission performance and fine ranging accuracy, a GS/s-sampling-rate analog-to-digital converter (ADC) and a high-speed digital baseband are required, which significantly decreases the system energy efficiency [16], [17]. On the contrary, the noncoherent UWB transceiver not only performs down-conversion through self-mixing but also employs a straightforward modulation scheme such as on–off keying (OOK). Not requiring the high-frequency phase-locked loop (PLL) and the high-speed ADC, the system energy efficiency is significantly improved. With their low-power and low-complexity architectures, noncoherent UWB transceivers are demanded for energy-efficient short-range wireless communications.

However, two major issues limit the development of conventional noncoherent UWB transceivers, which arise from baseband synchronization [18] and narrowband interference (NBI) [19]. In this work, we propose two techniques to address the major issues in UWB transceivers [20]. The first one is twin-OOK (T-OOK) modulation. The T-OOK signal employs a short-duration synchronization pulse as well as a long-duration data pulse with frequency hopping (FH), which not only eases baseband synchronization but also exhibits good spectrum efficiency [21] and link margin. The second one is the architecture of a quadrature uncertain-intermediate frequency (IF) receiver. By replacing the high-frequency PLL

Manuscript received 28 June 2023; revised 30 August 2023; accepted 23 September 2023. This article was approved by Associate Editor Minoru Fujishima. This work was supported by Tsinghua-Samsung joint research project. *(Corresponding author: Woogeun Rhee.)*

The authors are with the School of Integrated Circuits, Tsinghua University, Beijing 100084, China (e-mail: wbw18@mails.tsinghua.edu.cn; wrhee@tsinghua.edu.cn).

Color versions of one or more figures in this article are available at https://doi.org/10.1109/JSSC.2023.3322134.

Digital Object Identifier 10.1109/JSSC.2023.3322134

with an open-loop digital-controlled oscillator (DCO), the uncertain-IF architecture [19] inherits the low-power feature of the conventional noncoherent UWB receiver while maintaining a relatively good NBI tolerance. By combining the in-phase and quadrature (IQ) two-path signals, the proposed architecture also improves the ranging accuracy of the UWB system. With the proposed methods, a prototype 6–8-GHz sub-10-mW noncoherent UWB transceiver is implemented in 65-nm CMOS.

This article is organized as follows. Section II introduces the T-OOK modulation and the signal-design considerations. In Section III, the quadrature uncertain-IF receiver is discussed. Section IV presents the proposed transceiver implementation, followed by the measurement results in Section V. Finally, the conclusion is drawn in Section VI.

II. T-OOK MODULATION

A. Modulation Scheme

The T-OOK modulation is primarily proposed to address the baseband synchronization issue. Fig. 1 shows the basic concept of T-OOK in comparison to other modulation methods. Benefiting from its simple signal format, the OOK modulation shown in Fig. 1(a) is widely used in low-power UWB systems. However, baseband synchronization becomes problematic due to non-periodic pulses with a narrow pulsewidth. Even though Vigraham and Kinget [22] proposed a digital clock-and-data recovery (CDR) for baseband synchronization, a 32-bit preamble is required. Moreover, the CDR performance is degraded if a long sequence of data “0” appears. In order to ensure the CDR performance, redundant bits must be added to balance the data pattern. To simplify baseband synchronization in UWB systems, the synchronized-OOK (S-OOK) modulation is proposed [18], as shown in Fig. 1(b). Unlike the OOK modulation, an additional synchronization pulse is inserted before the OOK-based data pulse. This allows the transceiver to easily achieve baseband synchronization by detecting the synchronization pulse. The synchronization pulse, however, does not contain any data information but appears every symbol period. The system link margin is reduced by at least 3 dB due to the synchronization pulse.

Apart from baseband synchronization, the UWB spectrum mask limits the maximum transmitter power in both the OOK and the S-OOK modulations. To increase the maximum transmitter power, a pulse-shaping circuit should be implemented to improve the spectrum efficiency, which increases the transmitter design complexity and power consumption as well. In the T-OOK modulation, the durations of the synchronization pulse D_{SYN} and the data pulse D_{DATA} are different, as shown in Fig. 1(c). We employ a short-duration pulse for synchronization, while a long-duration data pulse with FH is employed to improve the system link margin. The short-duration synchronization pulse is located at the center frequency f_1. To satisfy the UWB spectrum mask, the carrier frequencies of the long-duration data pulses are hopped to reduce the peak level. The hopped carrier frequencies (f_2, f_3, $f_4, \ldots$) locate around f_1. By employing the FH method, the steep spectral roll-off of the narrowband data pulse improves the spectrum efficiency of the synchronization pulse. Therefore, the FH method not only ensures that the spectrum satisfies the spectrum mask but also enhances the spectrum efficiency. For ranging, the T-OOK signal is reconfigured into a conventional UWB signal, with only the short-duration synchronization pulse being transmitted. As a result, the ranging precision of the T-OOK signal is not affected by the long-duration data pulse.

In order to demodulate the T-OOK signal, a dual-path demodulation method is proposed, as shown in Fig. 2. Conventional baseband demodulation methods can be decomposed into envelope detection and energy detection. Envelope detection achieves a good timing resolution but is sensitive to high-frequency noise. On the other hand, energy detection offers robust demodulation but requires an accurately defined integration window. In this work, a dual-path demodulator architecture is proposed to leverage the benefits of both envelope detection and energy detection. The envelope detector detects the rising edge of the synchronization pulse and achieves baseband synchronization. The energy detector consists of an integrator and a threshold-tunable comparator. The synchronization controller SYN_CON and the window generator WIN_GEN create an integration window and a decision clock for the energy detector by comparing the synchronization pulse with the system baseband clock $\mathrm{CLK_{WIN}}$. The integration window is used by the integrator to integrate the data-pulse energy, and the decision clock is fed to the comparator for making data decisions. Since the synchronization pulse is only used for baseband synchronization, the misdetection of a few pulses does not degrade the overall sensitivity. On the contrary, each data pulse contains unique information. The bit-error-rate (BER) requirement of the data pulse is much stricter than that of the synchronization pulse. Accordingly, envelope detection is used to detect the synchronization pulse, while energy detection is used to detect the data pulse.

B. Signal-Design Considerations

To design a T-OOK signal, three aspects need to be considered. Those are the synchronization pulse, the data pulse, and the time interval between the synchronization pulse and the data pulse.

The first aspect is the synchronization pulse. The synchronization-pulse duration is determined by the T-OOK signal bandwidth. In this work, the synchronization pulse has a 4-ns duration with a null-to-null bandwidth of 500 MHz. In this case, the data-pulse spectrum is easy to fill the gap on either side of the main lobe of the synchronization-pulse spectrum, forming a spectrum-efficient T-OOK signal with a bandwidth of 500 MHz. If the synchronization-pulse duration is less than 4 ns, the T-OOK signal bandwidth will exceed 500 MHz. Therefore, a duration of 4 ns is the appropriate value for the synchronization pulse.

The second aspect that needs to be considered is the data pulse, including the pulse duration and the number of subbands. First, the data-pulse duration and the number of subbands are related to the spectrum efficiency. It is obvious that a longer pulse duration and a greater number of subbands

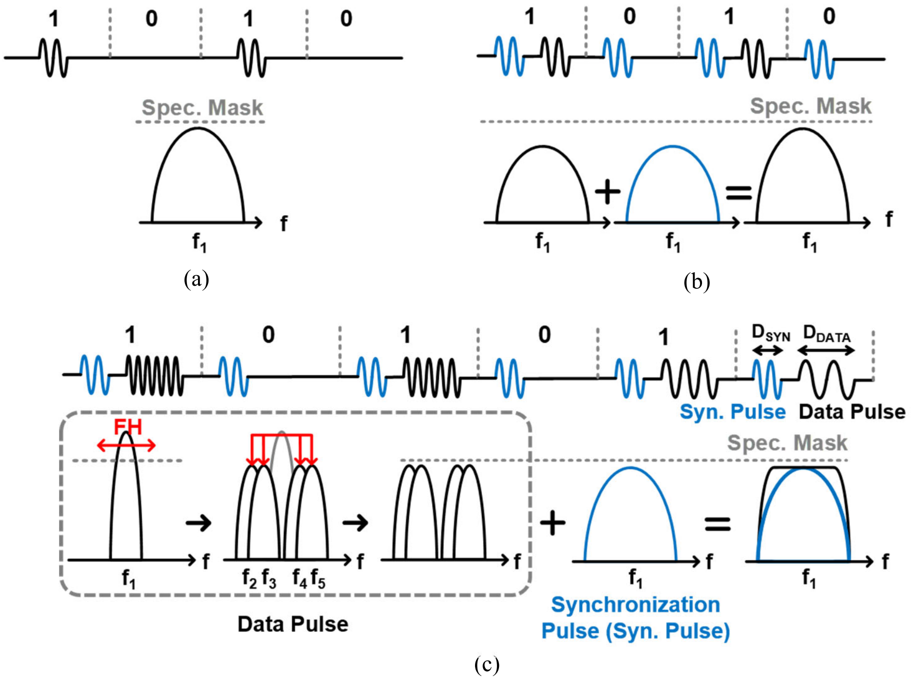

Fig. 1. OOK-based modulation schemes. (a) OOK. (b) S-OOK. (c) T-OOK.

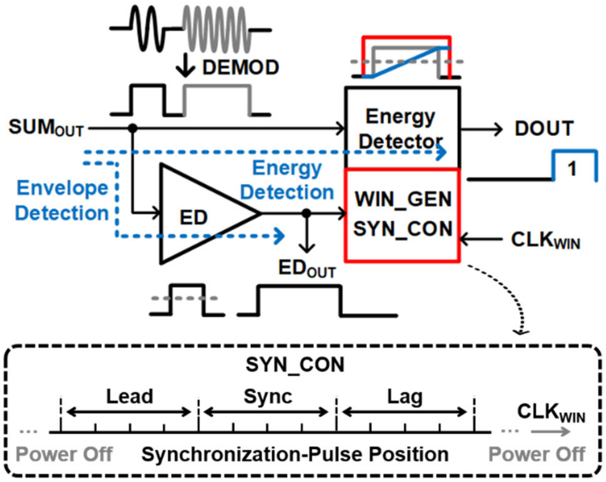

Fig. 2. Dual-path demodulation method for T-OOK signal.

shape the spectrum with a steep roll-off. However, a long-duration pulse contains more energy, which may result in the data-pulse spectrum exceeding the synchronization-pulse spectrum. In that case, achieving a flat in-band spectrum of the T-OOK signal becomes difficult, which significantly reduces the spectrum efficiency. To quantitatively analyze the spectrum efficiency, the power utilization ratio (PUR) is proposed, which is defined as the ratio of the in-band transmitter power $P_{\text{TX,IN-BAND}}$ to the ideal maximum power P_{MAX}, which is given by

$$\text{PUR} = \frac{P_{\text{TX,IN-BAND}}}{P_{\text{MAX}}}. \tag{1}$$

The ideal maximum power P_{MAX} is limited by the spectrum mask

$$P_{\text{MAX}} = -41.3\ \text{dBm/MHz} + 10\log(BW_{SIG}) \tag{2}$$

where the unit of the signal bandwidth (BW_{SIG}) is MHz. For a 500-MHz-bandwidth signal, the ideal maximum power P_{MAX} is -14.31 dBm. Fig. 3(a) and (b) shows the simulated T-OOK spectrums and PURs over different data-pulse durations and numbers of subbands, with a synchronization-pulse duration of 4 ns. It is clearly shown that the signal with 16 subbands has a better spectrum efficiency compared to the signal with 8 subbands.

Second, the data-pulse duration is also related to the system link margin. The synchronization pulse and data pulse are used for baseband synchronization and data demodulation, each with different signal-to-noise ratio (SNR) requirements. On one hand, if the data pulse has a similar duration to the synchronization pulse, the T-OOK signal closely resembles the S-OOK signal, which reduces the system link margin. On the other hand, if we continue to increase the data-pulse duration, the synchronization pulse will not be able to satisfy its SNR requirement because only a small portion of the total signal energy is allocated to the synchronization pulse. As a result, the baseband synchronization may be disrupted, ultimately limiting the overall demodulation performance.

In order to achieve the optimal link margin, the analysis of the BER for the T-OOK signal is conducted as follows. Envelope detection is used to detect the synchronization pulse. The BER for envelope detection on a pulsed-based signal should be analyzed first. Assuming that the demodulated pulse amplitude is V and the additive noise is narrowband Gaussian noise with a variance of σ_N^2, the SNR can be calculated as $E_b/N_0 = V^2/2\sigma_N^2$. We further assume that the threshold voltage of the envelope detector is $V_{T,\text{EV}}$ so that the normalized threshold voltage is given by $y_0 = V_{T,\text{EV}}/\sigma_N$. There are two possibilities for misdetection. The first possibility is that the envelope detector misjudges the symbol "0" as "1." This means that the transmitter does not send a pulse, but the

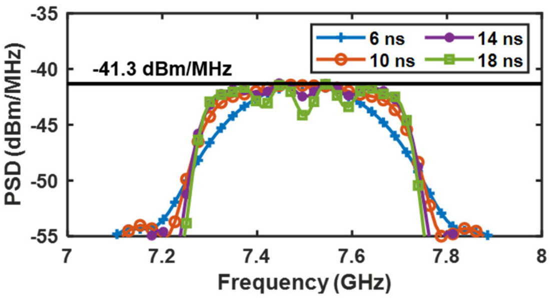

Data-Pulse Duration (ns)	6	10	14	18
PUR (dB)	-2.2	-1.5	-1.3	-1.7

(a)

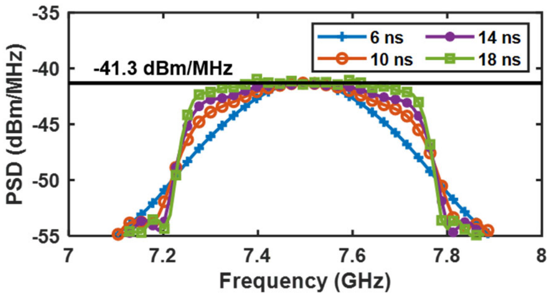

Data-Pulse Duration (ns)	6	10	14	18
PUR (dB)	-2.1	-1.4	-1.0	-0.5

(b)

Fig. 3. Simulated T-OOK spectrums over different data-pulse durations and numbers of subbands, with synchronization-pulse duration of 4 ns. (a) Eight subbands. (b) 16 subbands.

receiver mistakenly decides that a pulse has been received. The probability of misdetection without a transmitted signal $P_{b,\mathrm{EV}}(\mathrm{RX}|\overline{\mathrm{TX}})$ is given by [23]

$$P_{b,\mathrm{EV}}\left(\mathrm{RX}|\overline{\mathrm{TX}}\right) = e^{-\frac{y_0^2}{2}}. \tag{3}$$

It shows that the probability of this type of misdetection is only related to the normalized threshold voltage y_0. The probability decreases as y_0 increases. The second possibility for misdetection is that the envelope detection misjudges the symbol "1" as "0." This means that the transmitter sends a pulse, but the receiver fails to detect it. The probability of misdetection with a transmitted signal $P_{b,\mathrm{EV}}(\overline{\mathrm{RX}}|\mathrm{TX})$ is given by [23]

$$P_{b,\mathrm{EV}}\left(\overline{\mathrm{RX}}|\mathrm{TX}\right) = 1 - Q\left(\sqrt{\frac{2E_b}{N_o}}, y_0\right) \tag{4}$$

$$Q(\alpha, \beta) = \int_{\beta}^{\infty} t e^{-\frac{t^2+\alpha^2}{2}} I_0(\alpha t) dt \tag{5}$$

where $Q(\alpha, \beta)$ is called the Marcum Q-function and $I_0(x)$ is the modified first-kind Bessel function. We can observe that the probability of this type of misdetection is related to the normalized threshold voltage y_0 as well as the SNR E_b/N_0. The probability increases as y_0 increases.

Now, we move to the T-OOK signal. Equations (3) and (4) can be used to analyze the BER for envelope detection on the synchronization pulse. In the T-OOK signal, the synchronization-pulse position needs to be detected. The synchronization pulse falls into one of three position intervals, as shown in Fig. 2, representing the received signal leading, lagging, or being in sync with the system baseband clock $\mathrm{CLK_{WIN}}$. Correspondingly, there are three cases of misdetection on the synchronization pulse. The first case of misdetection is when the synchronization pulse leads the baseband clock, but the envelope detector fails to detect the pulse during the leading position interval. The BER for the synchronization pulse leading the baseband clock $P_{b,\mathrm{EV,LEAD}}$ is given by

$$P_{b,\mathrm{EV,LEAD}} = P_{b,\mathrm{EV}}\left(\overline{\mathrm{RX}}|\mathrm{TX}\right). \tag{6}$$

Similar to the first case, the second and third cases of misdetection on the synchronization pulse are also caused by the failure of the envelope detector to detect the synchronization pulse during the corresponding position intervals. It should be noted that the envelope detector is disabled for the remainder of the symbol period after detecting a pulse. As a result, the BERs for the synchronization pulse being in sync with the baseband clock $P_{b,\mathrm{EV,SYN}}$ and lagging the baseband clock $P_{b,\mathrm{EV,LAG}}$ are given by

$$\begin{aligned} P_{b,\mathrm{EV,SYN}} = {} & P_{b,\mathrm{EV}}\left(\mathrm{RX}|\overline{\mathrm{TX}}\right) \\ & + \left(1 - P_{b,\mathrm{EV}}\left(\mathrm{RX}|\overline{\mathrm{TX}}\right)\right) P_{b,\mathrm{EV}}\left(\overline{\mathrm{RX}}|\mathrm{TX}\right) \end{aligned} \tag{7}$$

$$\begin{aligned} P_{b,\mathrm{EV,LAG}} = {} & P_{b,\mathrm{EV}}\left(\mathrm{RX}|\overline{\mathrm{TX}}\right) \\ & + \left(1 - P_{b,\mathrm{EV}}\left(\mathrm{RX}|\overline{\mathrm{TX}}\right)\right) P_{b,\mathrm{EV}}\left(\mathrm{RX}|\overline{\mathrm{TX}}\right) \\ & + \left(1 - P_{b,\mathrm{EV}}\left(\mathrm{RX}|\overline{\mathrm{TX}}\right)\right)^2 P_{b,\mathrm{EV}}\left(\overline{\mathrm{RX}}|\mathrm{TX}\right). \end{aligned} \tag{8}$$

Equations (6)–(8) conclude the synchronization-pulse BER under different scenarios. Next, the data-pulse BER should be analyzed.

Energy detection is used to detect the OOK-based data pulse, which is the same as detecting an OOK signal. With the same assumption in the envelope-detection analysis, the demodulation performance of energy detection is related to the SNR E_b/N_0, the width of the integration window T_{int}, the receiver equivalent noise bandwidth BW_{RX}, and the threshold voltage $V_{T,EG}$. The BER $P_{b,EG}$ and the optimized threshold voltage $V_{T,EG}$ are [24]

$$P_{b,\mathrm{EG}} = Q\left(\frac{2\mu_\varepsilon(T_{\mathrm{int}})E_b/N_0}{\sqrt{M} + \sqrt{M + 4\mu_\varepsilon(T_{\mathrm{int}})E_b/N_0}}\right) \tag{9}$$

$$V_{T,\mathrm{EG}} = MN_0 + \frac{2\mu_\varepsilon(T_{\mathrm{int}})E_b\sqrt{MN_0^2}}{\sqrt{MN_0^2 + 4\mu_\varepsilon(T_{\mathrm{int}})E_b N_0} + \sqrt{MN_0^2}} \tag{10}$$

where $\mu_\varepsilon(T_{\mathrm{int}})$ represents the proportion of pulse energy within the integration window ($0 < \mu_\varepsilon(T_{\mathrm{int}}) < 1$). M, which is equal to the product of the integration-window width and the noise bandwidth ($T_{\mathrm{int}} \cdot BW_{RX}$), is used to measure the impact of integrated noise energy. From (9), the energy detection BER decreases as $\mu_\varepsilon(T_{\mathrm{int}})$ increases or M decreases.

Fig. 4 shows the BER comparison between the envelope detection on the synchronization pulse from (6) to (8) and the energy detection on the data pulse from (9). For the envelope detection, the normalized threshold voltage y_0 is set to 0.65. For the energy detection, $\mu_\varepsilon(T_{\mathrm{int}})$ is set to 0.8 and M is set to 1.

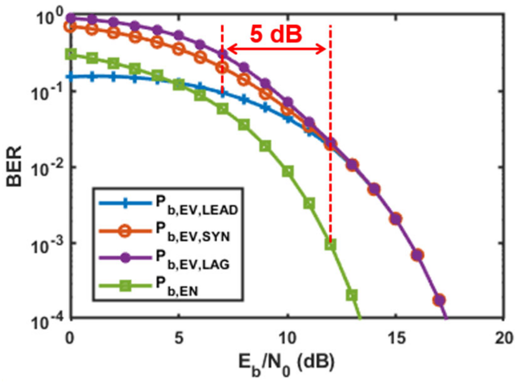

Fig. 4. Calculated BER performance of synchronization pulse and data pulse.

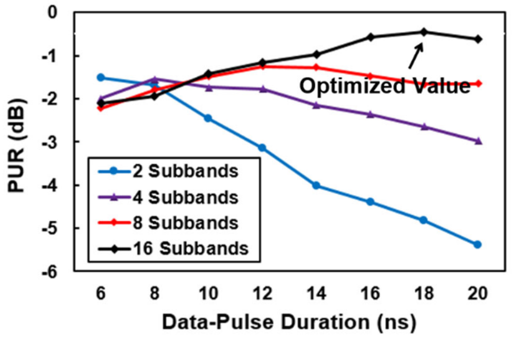

(a)

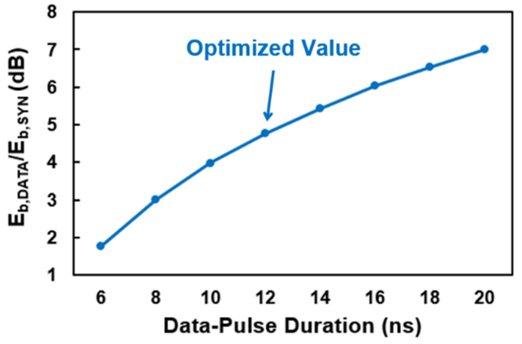

(b)

Fig. 5. Optimization of data-pulse duration with synchronization-pulse duration of 4 ns. (a) Spectrum-efficiency perspective. (b) Link-margin perspective.

Given that the baseband synchronization controller can achieve baseband synchronization with a synchronization-pulse BER of around 0.2, while the data-pulse BER should be less than 10^{-3}, the SNR requirement for the synchronization pulse is around 5 dB lower than that for the data pulse. To satisfy both BER requirements for the synchronization pulse and the data pulse, the data-pulse energy $E_{b,\mathrm{DATA}}$ should be 5 dB higher than the synchronization-pulse energy $E_{b,\mathrm{SYN}}$ to maximize the system link margin. As a result, the pulse energy ratio $E_{b,\mathrm{DATA}}/E_{b,\mathrm{SYN}}$ is a critical parameter used to design a T-OOK signal from the perspective of the system link margin.

Fig. 5 summarizes the PUR and the pulse energy ratio $E_{b,\mathrm{DATA}}/E_{b,\mathrm{SYN}}$ of different T-OOK signals with a 4-ns synchronization-pulse duration. A T-OOK signal with 16 subbands and a data-pulse duration of 18 ns is chosen in this work. The signal offers the best spectrum efficiency (PUR $= -0.46$ dB) and a moderate system link margin ($E_{b,\mathrm{DATA}}/E_{b,\mathrm{SYN}} = 6.53$ dB).

The last signal-design consideration is the time interval between the synchronization pulse and the data pulse. The time interval is primarily determined by the maximum data rate and the presence of multipath interference. If the time interval is too short, the multipath interference caused by the synchronization pulse will affect the data pulse. On the other hand, the maximum data rate of this work is 10 Mb/s and the symbol period is only 100 ns. If the time interval is too long, the multipath interference caused by the data pulse will affect the synchronization pulse in the next symbol. Therefore, the time interval should be chosen carefully. It seems that the time interval should be half the symbol period to maximize the interval and suppress the multipath interference caused by different pulses. However, two additional points need further consideration. First, the durations of the two types of pulses are different. The synchronization-pulse duration is much shorter than the data-pulse duration. Second, the synchronization pulse is detected through envelope detection, while the data pulse is detected through energy detection. Energy detection is more robust against interference than envelope detection. As a result, the multipath interference caused by the synchronization pulse is less severe than that caused by the data pulse. Based on the above points, the time interval between the synchronization pulse and the data pulse is set to 28 ns in this work, leaving a time interval of 50 ns between the data pulse and the next-bit synchronization pulse.

III. QUADRATURE UNCERTAIN-IF ARCHITECTURE

The self-mixing-based noncoherent UWB receiver achieves low-power and low-complexity demodulation but is vulnerable to NBI. In [19], an uncertain-IF architecture is employed for the UWB receiver to achieve a good NBI tolerance. Fig. 6 shows the basic concept of the uncertain-IF receiver. In the receiver, an RF signal is first down-converted to a specific range of an IF using a mixer and then further down-converted to a baseband signal using a squarer. Since the squarer can tolerate frequency uncertainty, a high-frequency PLL can be replaced with a roughly calibrated oscillator. In addition, the bandpass filter (BPF) at the IF stage provides an additional filtering effect to the NBI compared to the conventional noncoherent receiver. In the narrowband receiver [25], the uncertain-IF architecture requires an off-chip high-Q RF filter to reject nearby interferers in the crowded ISM band due to the IF uncertainty. Besides, precise control of the LO-signal frequency is critical in the narrowband receiver as well. In the UWB receiver, a wide signal bandwidth with a generous guard band enables the use of an on-chip RF amplifier (RFA) instead of an off-chip RF filter. In addition, the design complexities of the LO generator and the IF filter are also reduced. As the high-frequency PLL is replaced with an open-loop oscillator, the uncertain-IF receiver greatly simplifies the overall transceiver architecture and improves the system energy efficiency.

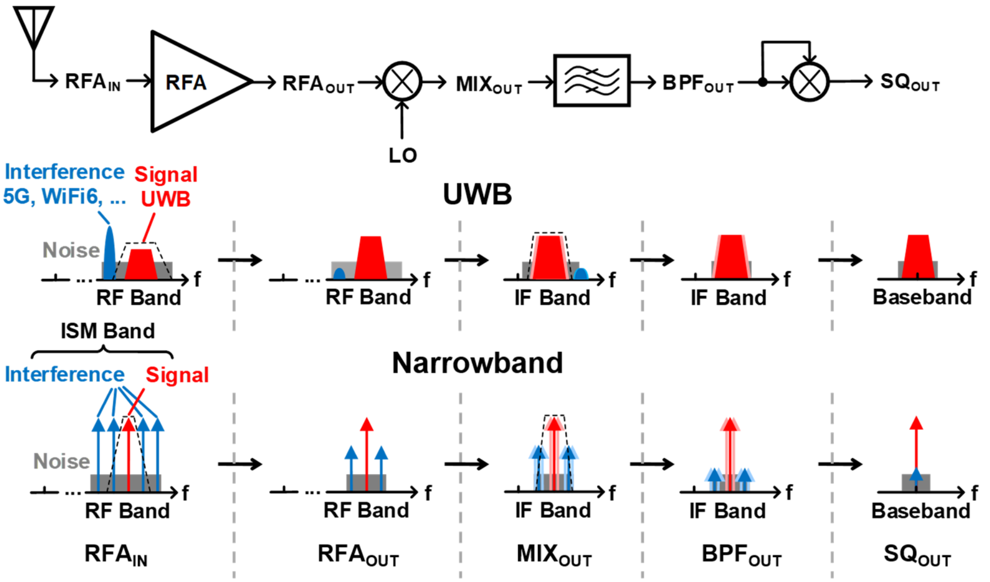

Fig. 6. Uncertain-IF receiver comparison between UWB and narrowband communication.

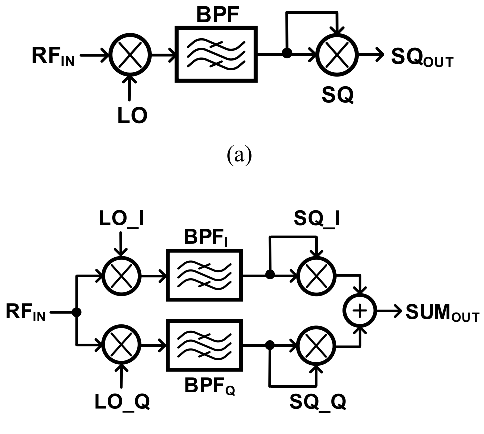

(a)

(b)

Fig. 7. Block diagram of uncertain-IF receiver. (a) Conventional uncertain-IF receiver. (b) Quadrature uncertain-IF receiver.

Fig. 7(a) shows the block diagram of a conventional uncertain-IF receiver. The input RF signal RF_{IN} is

$$RF_{IN} = \sin(\omega_c t) \cdot p(t) \tag{11}$$

$$p(t) = u(t) - u(t - \tau) \tag{12}$$

where $p(t)$ represents a square pulse envelope and $u(t)$ is the step function. The LO signal LO is

$$LO = \sin[(\omega_{\mathrm{LO}} + \omega_0)t + \varphi_0] \tag{13}$$

where ω_0 is the LO-signal frequency offset between the current frequency and the ideal frequency. φ_0 is the LO-signal phase offset between the current phase and the ideal phase. The output signal of the mixer $MIXER_{OUT}$ is

$$\begin{aligned} MIXER_{OUT} &= RF_{IN} \cdot LO \\ &= \frac{1}{2}\Big\{\cos[(\omega_{\mathrm{IF}} - \omega_0)t - \varphi_0] \\ &\quad - \cos[(2\omega_{\mathrm{LO}} + \omega_{\mathrm{IF}} + \omega_0)t + \varphi_0]\Big\} \cdot p(t) \end{aligned} \tag{14}$$

where $\omega_{\mathrm{IF}} = \omega_c - \omega_{\mathrm{LO}}$ is the IF value. After the BPF, the high-frequency component is filtered out and the output signal of the BPF BPF_{OUT} is

$$BPF_{OUT} = \frac{1}{2}\cos[(\omega_{\mathrm{IF}} - \omega_0)t - \varphi_0] \cdot p(t). \tag{15}$$

The squarer output SQ_{OUT} is the baseband signal, which is given by

$$SQ_{OUT} = \frac{1}{8}\{\cos[2(\omega_{\mathrm{IF}} - \omega_0)t - 2\varphi_0] + 1\} \cdot p(t)^2. \tag{16}$$

From (16), the squarer output contains both the dc component and the 2nd-order-harmonic component. An LPF needs to be used to filter out the 2nd-order-harmonic component, leaving only $p(t)^2/8$ in the ideal case. However, the 2nd-order-harmonic component cannot be completely filtered in practice. The remaining 2nd-order-harmonic component modulates the rising edge of the demodulated pulse and introduces rising-edge jitter, which degrades the accuracy of time-of-flight (TOF) ranging. Hence, choosing a relatively high IF is desirable to relax the LPF requirement and minimize the degradation of ranging accuracy. In addition, having a high IF is beneficial for mitigating image interference in the conventional uncertain-IF architecture. As a result, a high IF of 1.5 GHz is chosen in [19].

In this work, we propose a quadrature uncertain-IF architecture, as shown in Fig. 7(b). Similar to the derivation in the conventional uncertain-IF architecture, the input signal RF_{IN} and the quadrature LO signals LO_I and LO_Q are

$$RF_{IN} = \sin(\omega_c t) \cdot p(t) \tag{17}$$

$$LO\_I = \sin[(\omega_{\mathrm{LO}} + \omega_0)t + \varphi_0] \tag{18}$$

$$LO\_Q = \cos[(\omega_{\mathrm{LO}} + \omega_0)t + \varphi_0]. \tag{19}$$

The quadrature mixers down-convert the input signal to the dual-path IF signals, and the BPFs limit the IF-signal bandwidth. The output signals of the BPFs BPF_I_{OUT} and

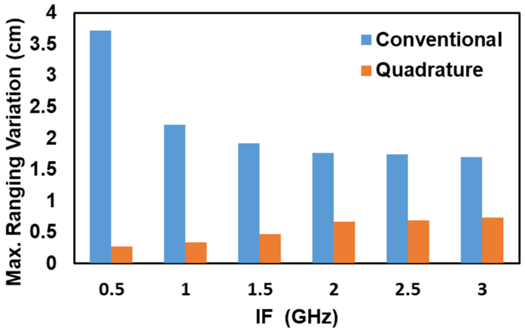

Fig. 8. Comparison of ranging accuracy between conventional uncertain-IF architecture and quadrature uncertain-IF architecture using different IFs.

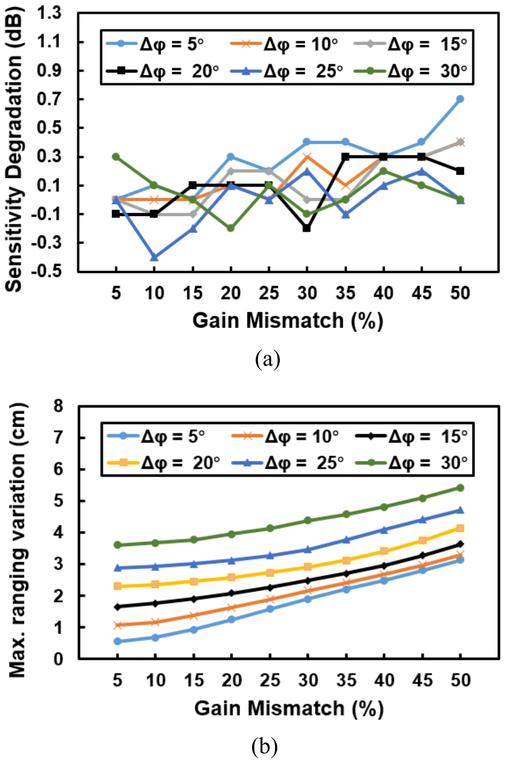

Fig. 9. Effect of IQ mismatch on quadrature uncertain-IF architecture. (a) Sensitivity degradation. (b) Maximum ranging variation.

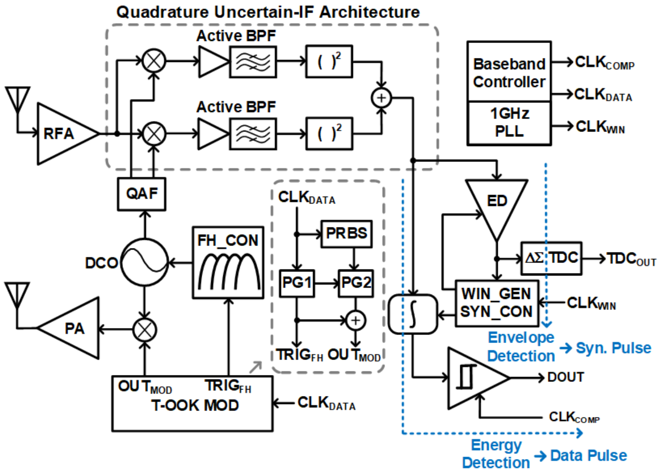

Fig. 10. Proposed transceiver block diagram.

BPF_Q_{OUT} are given as follows:

$$BPF\_I_{OUT} = \frac{1}{2}\cos[(\omega_{\mathrm{IF}} - \omega_0)t - \varphi_0] \cdot p(t) \tag{20}$$

$$BPF\_Q_{OUT} = \frac{1}{2}\sin[(\omega_{\mathrm{IF}} - \omega_0)t - \varphi_0] \cdot p(t). \tag{21}$$

After the squares and the summer, the baseband signal SUM_{OUT} is

$$SUM_{OUT} = BPF\_I_{OUT}^2 + BPF\_Q_{OUT}^2 = \frac{1}{4}p(t)^2. \tag{22}$$

From (22), it is easy to observe that by combining the IQ-path signals, the quadrature uncertain-IF architecture does not suffer from the 2nd-order-harmonic problem present in the conventional uncertain-IF architecture. Fig. 8 shows a comparison of the ranging accuracy between the conventional uncertain-IF architecture and the quadrature uncertain-IF architecture with different IFs. The ranging variation is calculated by measuring the time interval between the rising edges of the demodulated pulses with different phases of the input signal. Caused by different phases, the maximum ranging variation of the conventional uncertain-IF architecture increases with a low IF, while the quadrature uncertain-IF architecture maintains almost the same ranging variation with different IFs. As a result, a zero IF is chosen to reduce power consumption and circuit design complexity in the quadrature uncertain-IF architecture. In addition, the zero-IF architecture does not suffer from image interference. Due to the wide signal bandwidth, the dc offset and $1/f$ noise can be directly filtered out by the BPF. However, eliminating the frequency mismatch between the transmitter and the receiver is challenging due to the open-loop oscillator. Therefore, the zero IF becomes a close-to-zero IF in practice.

For the quadrature uncertain-IF architecture, one potential issue is the IQ mismatch. Fig. 9(a) shows the sensitivity degradation caused by IQ mismatch. The sensitivity is measured at BER $= 10^{-3}$. We assume that there is an additive white Gaussian noise (AWGN) channel between the transmitter and the receiver. It is evident that if we can control the IQ gain mismatch to be less than 50% and the phase mismatch to be less than 30°, the sensitivity degradation will be less than 1 dB. Compared to the sensitivity, the ranging accuracy is more sensitive to the IQ mismatch, as shown in Fig. 9(b). If the IQ gain mismatch is less than 15% and the phase mismatch is less than 5°, the maximum ranging variation caused by different phases of the input signal will be less than 1 cm, which can be easily achieved with a calibrated all-pass filter (QAF). In addition, since the phases of an input signal at different times are almost random, the ranging accuracy can be further improved by oversampling. The oversampling operation is done by a $\Delta\Sigma$ time-to-digital converter (TDC) [26], which will be discussed in Section IV.

IV. TRANSCEIVER IMPLEMENTATION

Fig. 10 shows the block diagram of the proposed architecture. The transmitter employs a conventional DCO-based

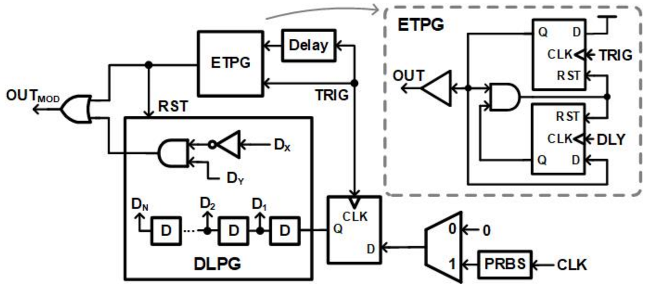

Fig. 11. T-OOK modulator block diagram.

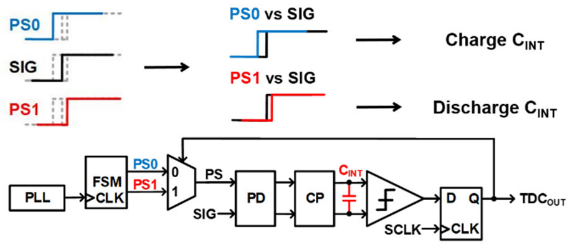

Fig. 12. ΔΣ TDC block diagram.

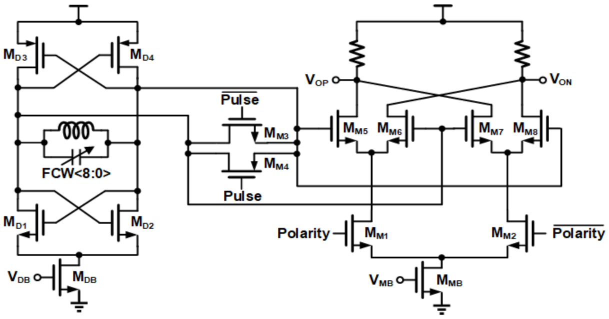

Fig. 13. DCO and mixer schematic.

architecture. The LO signal directly up-converts the T-OOK baseband signal to the RF signal. The T-OOK modulator *T-OOK MOD* generates the T-OOK baseband signal, and the FH controller *FH_CON* controls the center frequencies of each data pulse. The receiver front end is based on the quadrature uncertain-IF architecture. Based on the previous analysis, a close-to-zero IF is chosen to minimize power consumption and simplify circuit designs. An open-loop DCO, replacing the high-frequency PLL, serves as the LO generator. The IQ LO signals are separated by a quadrature QAF. The active BPF is used not only to suppress the LO leakage and $1/f$ noise but also to provide variable gains. The IQ signals are combined into the baseband signal by a summer. The demodulated T-OOK signal is detected using the dual-path architecture, where the synchronization pulse and the data pulse are detected by envelope detection and energy detection, respectively. The synchronization controller achieves baseband synchronization by using the output of the envelope detector. It generates the integration window and the decision clock for the energy detector. The envelope-detector output is directly fed to a ΔΣ TDC for fine ranging. The ΔΣ TDC achieves picosecond-level time resolution with a 1-bit oversampled output. A 1-GHz PLL with a ring voltage-controlled oscillator (VCO) produces baseband clocks at various frequencies.

Fig. 11 shows the block diagram of the T-OOK modulator. The T-OOK modulator consists of an edge-triggered pulse generator (ETPG) and a delay-line-based pulse generator (DLPG). The ETPG generates the synchronization pulse with a fixed duration introduced by a fixed delay cell. The DLPG generates the data pulse by combining two delay-cell outputs. The data-pulse duration, as well as the time interval between the synchronization and the data pulses, is determined by selecting different delay-cell outputs with a step of 2 ns. The ΔΣ TDC block diagram is shown in Fig. 12. The ΔΣ TDC consists of a phase detector (PD), a charge pump (CP), an integration capacitor C_{INT}, a comparator, a D-type flip-flop (DFF), and a multiplexer. The 1-GHz PLL with the finite-state machine (FSM) generates two reference signals, $PS0$ and $PS1$. By comparing the phase differences between the reference signals and the demodulated signal, C_{INT} is either charged or discharged. After that, the comparator quantifies the integration voltage and outputs 1-bit data. By averaging the 1-bit-data stream, the noise-filtering feature can be achieved in the ΔΣ TDC. Fig. 13 shows the schematic of the DCO and the mixer in the transmitter. Complementary cross-coupled pairs M_{D1}–M_{D4} are utilized in the *LC* DCO to achieve both good noise performance and a short startup time. The *LC* DCO achieves a phase noise of −94 dBc/Hz at a 1-MHz offset for a 7.5-GHz output. With an 8-bit binary-weighted frequency control word FCW⟨7:0⟩ and a redundant bit FCW⟨8⟩, the DCO achieves a frequency resolution of 10 MHz/LSB. The Gilbert-type mixer is designed for up-conversion. Random binary-phase shift keying (BPSK) modulation is applied to eliminate the discrete spectral spurs of the RF signal [13]. Fig. 14 shows the schematic of the RFA. The RFA is a two-stage wideband amplifier that achieves a 500-MHz bandwidth with a center-frequency tuning range of 6.3–8.6 GHz. The noise figure (NF) and the input 3rd-order intercept point (IIP3) of the RFA are 8.5 dB and −15.2 dBm, respectively. A 4-bit binary-weighted current control word GCW⟨3:0⟩ is used to adjust the gain of the amplifier within the range of 22.6–31.8 dB. The QAF shown in Fig. 15 contains a 2-bit resistor array RCW⟨1:0⟩ and a 4-bit capacitor array CCW⟨3:0⟩ to achieve amplitude and phase trimming steps of 100 mV and 5°, respectively. Two additional resistors R_S, with the parasitic resistance of the capacitor array, mitigate the capacitive loading and minimize the IQ amplitude and phase mismatch [27]. Fig. 16 shows the schematic of the active BPF [15]. The input high-pass network has a tunable corner frequency of 1–30 MHz with the control word $S\langle 2{:}0\rangle$. The low-pass network is implemented at the output of the BPF with a typical corner frequency of 300 MHz, providing a 50-MHz margin for the IF uncertainty. A source-degeneration resistor array TC⟨4:0⟩ is used to achieve the gain control of 9.2–20.5 dB. The comparator in the receiver baseband employs a double cross-coupled pair to achieve a high voltage gain [28]. A current-steering digital-to-analog converter (DAC) is designed to adjust the threshold voltage by changing the differential-pair bulk voltage.

TABLE I
PERFORMANCE SUMMARY AND COMPARISON

		This Work	**[14]**	**[17]**	**[18]**	**[19]**	**[29]**
Process		65-nm CMOS	130-nm CMOS	40-nm CMOS + 130-nm SOI	90-nm CMOS	65-nm CMOS	130-nm CMOS
Architecture		Uncertain-IF	Coherent	Coherent	Noncoherent	Uncertain-IF	Noncoherent
Application$^{(1)}$		C & R	C & R	C & R	C	C & R	C
Area (mm^2)		3.42	5.8	10.5	0.6$^{(2)}$	3.75	0.55$^{(2)}$
Modulation		T-OOK	BPSK	BPM + BPSK	S-OOK	S-OOK	PPM
RF Band (GHz)		6.0-8.0	3.0-5.0	6.5-10	3.6-4.3	7.25-7.75	7.25-8.5
Data Rate (Mb/s)		10	1	0.85	1	5	4.4
Power (mW)	**TX**	3.83	N/A	61.6	0.258	5.93	N/A
	RX	5.38	50	150	2.18		1.9
Energy Efficiency (nJ/b)	**TX**	0.38	N/A	72.5	0.26	1.2	N/A
	RX	0.54	50	176	1.45		0.44
Ranging Accuracy (cm)		0.96$^{(3)}$	0.25	1	N/A	1.46$^{(3)}$	N/A
Sensitivity (dBm)		-71 @ 10 Mb/s	-95 @ 1 Mb/s	-99 @ 0.85 Mb/s$^{(4)}$	-66 @ 1 Mb/s	-77 @ 1 Mb/s	-86 @ 4.4 Mb/s
Sensitivity Scaled to 1 Mb/s (dBm)		-81	-95	-98$^{(4)}$	-66	-77	-92
NBI Tolerance (dBm) / NBI Frequency (GHz)		-22.4$^{(5)}$ / 6	N/A	-40 / 5.8	-21 / 2.4	-23.8 / 6	-45 / 6

$^{(1)}$ C: communication, R: ranging $^{(2)}$ Active area $^{(3)}$ Rms error $^{(4)}$ BER = 0.1 $^{(5)}$ Measured at 7.5-GHz band

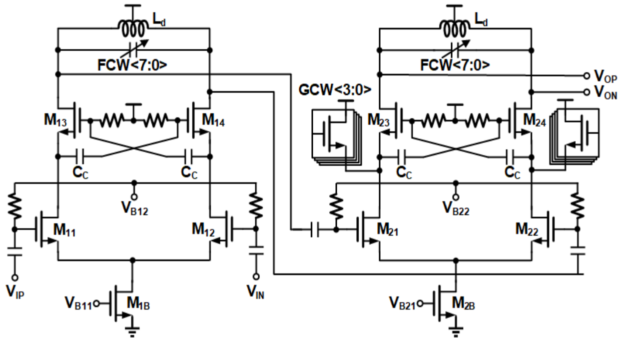

Fig. 14. RFA schematic.

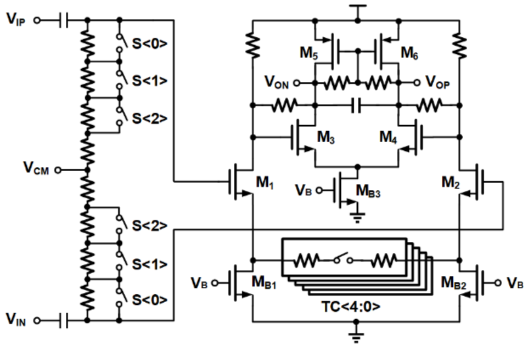

Fig. 16. Active BPF schematic.

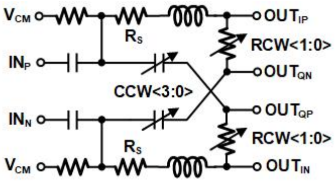

Fig. 15. QAF schematic.

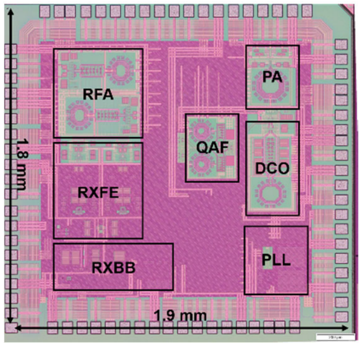

Fig. 17. Chip micrograph.

V. MEASUREMENT RESULTS

A prototype T-OOK transceiver is implemented in 65-nm CMOS. A chip micrograph is shown in Fig. 17. The die area, including pads, is 1.9 mm × 1.8 mm. The measured DCO tuning range is 5.7–8.0 GHz, as shown in Fig. 18. The highest bit of the DCO control word serves as a redundant bit to compensate for process variation. Fig. 19(a) and (b) shows the measured transmitter spectrum and waveform with a data rate of 10 Mb/s. The T-OOK signal contains 16 subbands,

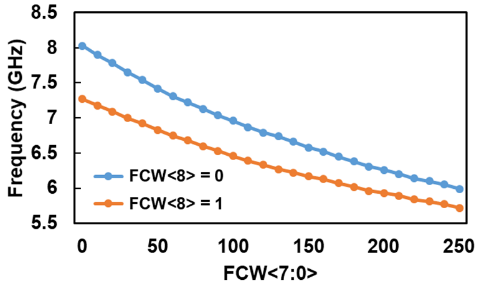

Fig. 18. Measured DCO tuning range.

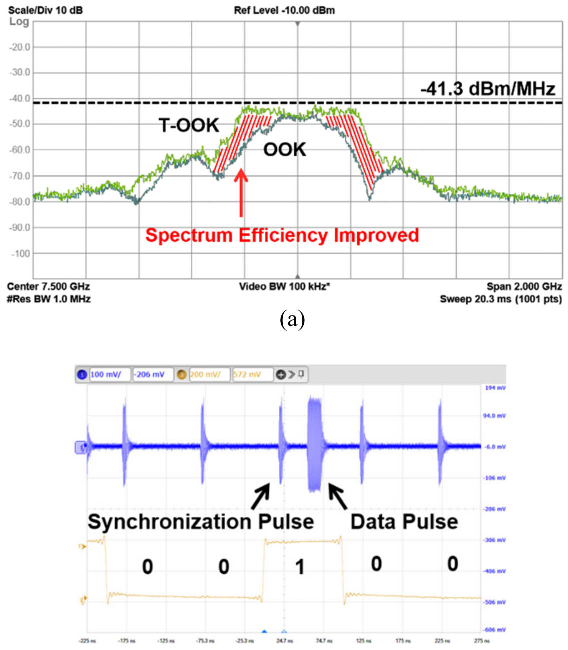

(a)

(b)

Fig. 19. Measured transmitter performance. (a) Spectrum comparison between T-OOK and OOK. (b) Transient waveform.

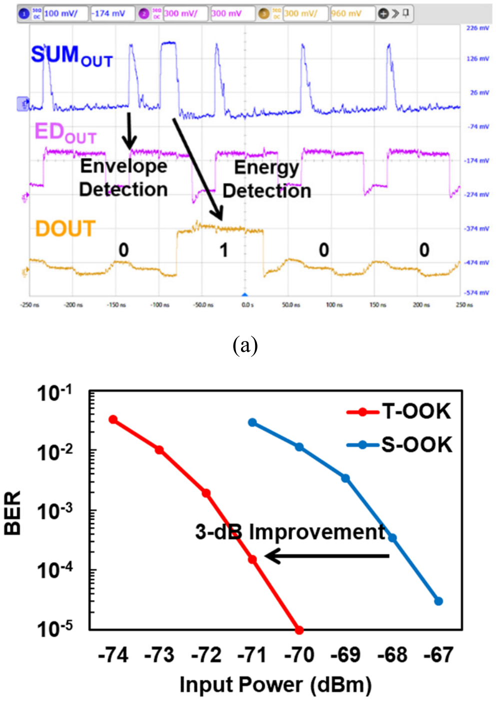

(a)

(b)

Fig. 20. Measured demodulation performance. (a) Demodulation waveform. (b) Sensitivity comparison between T-OOK and S-OOK.

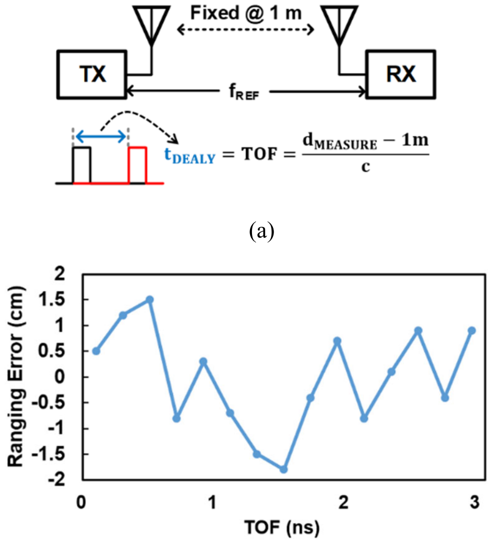

(a)

(b)

Fig. 21. Measured ranging performance. (a) Measurement setup. (b) Ranging error when the TOF varies from 0 to 3 ns.

and the synchronization pulse and data pulse have durations of 4 and 18 ns, respectively. Also, an OOK signal with a duration of 4 ns is generated for comparison. Due to the FH method, the T-OOK signal exhibits a fairly flat passband and a steep roll-off, verifying better spectrum efficiency compared to the OOK signal. Fig. 20 shows the measured receiver performance. The center frequency is set at 7.5 GHz. The demodulated waveforms of the synchronization pulse and the data pulse are shown in Fig. 21(a), as detected by the envelope detector and the energy detector. To verify the improvement in the link margin of the T-OOK modulation, we compare the receiver sensitivity of the T-OOK signal and the S-OOK signal. The T-OOK signal and the S-OOK signal are generated by an arbitrary waveform generator (Tektronix AWG70001B). A tunable attenuator is inserted between the transmitter and the receiver to adjust the input power levels. For the T-OOK signal, the receiver achieves a sensitivity of −71 dBm at 10 Mb/s, while it is −68 dBm for the S-OOK signal, as shown in Fig. 21(b). To measure the NBI tolerance, a 7.5-GHz T-OOK signal with a 10-Mb/s data rate and a −70-dBm power is used as an input signal. In addition, a 6-GHz BPSK signal with a 20-MHz bandwidth is used as the interference, emulating the 802.11a Wi-Fi signal. The receiver achieves an NBI tolerance of −22.4 dBm with 1-dB sensitivity degradation.

The ranging measurement setup is shown in Fig. 21(a), where d_{MEASURE} represents the distance to be measured and c is the speed of electromagnetic wave propagation. The actual distance between the transmitter and the receiver is fixed at 1 m. To prevent reference frequency mismatch between the transmitter and the receiver, both devices use the same reference clock f_{REF}. A pulse-position-modulation (PPM) method is utilized to emulate different actual distances on the transmitter side. The portion of d_{MEASURE} that exceeds 1 m is emulated by transmitting pulses with a time delay t_{DELAY}. In this work, the pulse position is accurately controlled with a time step of 200 ps. A TOF resolution of 200 ps is equivalent to an actual distance of 6 cm. The $\Delta\Sigma$ TDC relaxes the PLL jitter requirement by oversampling. The 1-GHz baseband PLL achieves a phase noise of −84.7 dBc/Hz at 1-MHz offset with a power consumption of less than 500 μW. Benefiting from the quadrature uncertain-IF architecture and the $\Delta\Sigma$ TDC, the transceiver achieves a root-mean-square (rms) ranging error of 0.96 cm with a pulse repeat frequency (PRF) of 1 MHz when the TOF varies from 0 to 3 ns, as shown in Fig. 21(b).

Table I shows the measured performance summary in comparison with other recent UWB transceivers or receivers. The proposed transceiver has both communication and ranging modes. In the communication mode, the transceiver has a sensitivity of −71 dBm at 10 Mb/s and an NBI tolerance of −22.4 dBm for 6-GHz interference. In the ranging mode, the transceiver achieves an rms ranging accuracy of 0.96 cm. With the T-OOK modulation and the quadrature uncertain-IF demodulation, the proposed transceiver overcomes the disadvantages of the conventional noncoherent architecture in terms of baseband synchronization, spectrum efficiency, NBI tolerance, and fine ranging while also inheriting the low-power and low-complexity features.

VI. Conclusion

A T-OOK UWB transceiver with the quadrature uncertain-IF receiver architecture is implemented in 65-nm CMOS. With the proposed T-OOK modulation, the transceiver not only achieves baseband synchronization efficiently but also obtains good spectrum efficiency and system link margin. With the quadrature uncertain-IF architecture, the receiver inherits the low-power and low-complexity features of the noncoherent receiver while maintaining a relatively good NBI tolerance. The transceiver achieves a sensitivity of −71 dBm at 10 Mb/s and an rms ranging accuracy of 0.96 cm. The transmitter and the receiver have power consumption of 3.83 and 5.38 mW, respectively.

References

[1] K. Shibata et al., "A 22 nm 0.84 mm^2 BLE transceiver with self IQ-phase correction achieving 39 dB image rejection and on-chip antenna impedance tuning," in *IEEE Int. Solid-State Circuits Conf. (ISSCC) Dig. Tech. Papers*, vol. 65, Feb. 2022, pp. 398–400.

[2] Z. Sun et al., "A 0.85 mm^2 BLE transceiver using an on-chip harmonic-suppressed RFIO circuitry with T/R switch," *IEEE Trans. Circuits Syst. I, Reg. Papers*, vol. 68, no. 1, pp. 196–209, Jan. 2021.

[3] M. Ding et al., "A Bluetooth 5 transceiver with a phase-tracking RX and its corresponding digital baseband in 40-nm CMOS," *IEEE J. Solid-State Circuits*, vol. 56, no. 1, pp. 254–266, Jan. 2021.

[4] M. Tamura et al., "A 0.5-V BLE transceiver with a 1.9-mW RX achieving −96.4-dBm sensitivity and −27-dBm tolerance for intermodulation from interferers at 6- and 12-MHz offsets," *IEEE J. Solid-State Circuits*, vol. 55, no. 12, pp. 3376–3386, Dec. 2020.

[5] M. Ding et al., "A 0.8 V 0.8 mm^2 Bluetooth 5/BLE digital-intensive transceiver with a 2.3 mW phase-tracking RX utilizing a hybrid loop filter for interference resilience in 40 nm CMOS," in *IEEE Int. Solid-State Circuits Conf. (ISSCC) Dig. Tech. Papers*, Feb. 2018, pp. 446–448.

[6] H. Liu et al., "An ADPLL-centric Bluetooth low-energy transceiver with 2.3 mW interference-tolerant hybrid-loop receiver and 2.9 mW single-point polar transmitter in 65 nm CMOS," in *IEEE Int. Solid-State Circuits Conf. (ISSCC) Dig. Tech. Papers*, Feb. 2018, pp. 444–446.

[7] C. Lu, S.-L. Chen, J. Liu, J. Bao, Y. Wang, and Y. Zhao, "Dual-band 802.11ax transceiver design with 1024-QAM and 160-MHz CBW support," *IEEE Solid-State Circuits Lett.*, vol. 6, pp. 137–140, 2023.

[8] E. Lu et al., "A 4×4 dual-band dual-concurrent WiFi 802.11ax transceiver with integrated LNA, PA and T/R switch achieving +20dBm 1024-QAM MCS11 pout and −43dB EVM floor in 55 nm CMOS," in *IEEE Int. Solid-State Circuits Conf. (ISSCC) Dig. Tech. Papers*, Feb. 2020, pp. 178–180.

[9] S. Kawai et al., "An 802.11ax 4 × 4 high-efficiency WLAN AP transceiver SoC supporting 1024-QAM with frequency-dependent IQ calibration and integrated interference analyzer," *IEEE J. Solid-State Circuits*, vol. 53, no. 12, pp. 3688–3699, Dec. 2018.

[10] J. Lei et al., "A 1.8 Gb/s, 2.3 pJ/bit, crystal-less IR-UWB transmitter for neural implants," in *IEEE Int. Solid-State Circuits Conf. (ISSCC) Dig. Tech. Papers*, Feb. 2023, pp. 464–466.

[11] M. Song, Y. Huang, H. J. Visser, J. Romme, and Y.-H. Liu, "An energy-efficient and high-data-rate IR-UWB transmitter for intracortical neural sensing interfaces," *IEEE J. Solid-State Circuits*, vol. 57, no. 12, pp. 3656–3668, Dec. 2022.

[12] G. Lee, J. Jang, J.-H. Kim, and T. W. Kim, "An IR-UWB CMOS transceiver with extended pulse position modulation," *IEEE J. Solid-State Circuits*, vol. 57, no. 8, pp. 2281–2291, Aug. 2022.

[13] H. Song, Z. Ding, W. Rhee, and Z. Wang, "A secure TOF-based transceiver with low latency and sub-cm ranging for mobile authentication applications," in *Proc. IEEE Radio Freq. Integr. Circuits Symp. (RFIC)*, Jun. 2018, pp. 160–163.

[14] D. Morche et al., "Double-quadrature UWB receiver for wide-range localization applications with sub-cm ranging precision," *IEEE J. Solid-State Circuits*, vol. 48, no. 10, pp. 2351–2362, Oct. 2013.

[15] H. Song, D. Liu, Y. Zhang, W. Rhee, and Z. Wang, "A 6.5–8.1-GHz communication/ranging VWB transceiver for secure wireless connectivity with enhanced bandwidth efficiency and energy detection," *IEEE J. Solid-State Circuits*, vol. 55, no. 2, pp. 219–232, Feb. 2020.

[16] W. Kim et al., "A fully integrated IEEE 802.15.4/4z-compliant 6.5-to-8 GHz UWB system-on-chip RF transceiver supporting precision positioning in a CMOS 28 nm process," in *IEEE Int. Solid-State Circuits Conf. (ISSCC) Dig. Tech. Papers*, Feb. 2023, pp. 462–464.

[17] R. Chen et al., "A 6.5-to-10 GHz IEEE 802.15.4/4z-compliant 1T3R UWB transceiver," in *IEEE Int. Solid-State Circuits Conf. (ISSCC) Dig. Tech. Papers*, vol. 65, Feb. 2022, pp. 396–398.

[18] M. Crepaldi, C. Li, J. R. Fernandes, and P. R. Kinget, "An ultra-wideband impulse-radio transceiver chipset using synchronized-OOK modulation," *IEEE J. Solid-State Circuits*, vol. 46, no. 10, pp. 2284–2299, Oct. 2011.

[19] B. Wang, H. Song, W. Rhee, and Z. Wang, "A 7.25–7.75 GHz 5.9 mW UWB transceiver with −23.8 dBm NBI tolerance and 1.5 cm ranging accuracy using uncertain IF and pulse-triggered envelope/energy detection," in *Proc. IEEE Custom Integr. Circuits Conf. (CICC)*, Apr. 2022, pp. 1–2.

[20] B. Wang, W. Rhee, and Z. Wang, "A quadrature uncertain-IF IR-UWB transceiver with twin-OOK modulation," in *IEEE Int. Solid-State Circuits Conf. (ISSCC) Dig. Tech. Papers*, Feb. 2023, pp. 1–3.

[21] D. Liu, X. Ni, R. Zhou, W. Rhee, and Z. Wang, "A 0.42-mW 1-Mb/s 3-to 4-GHz transceiver in 0.18-μm CMOS with flexible efficiency, bandwidth, and distance control for IoT applications," *IEEE J. Solid-State Circuits*, vol. 52, no. 6, pp. 1479–1494, Jun. 2017.

[22] B. Vigraham and P. R. Kinget, "A self-duty-cycled and synchronized UWB pulse-radio receiver SoC with automatic threshold-recovery based demodulation," *IEEE J. Solid-State Circuits*, vol. 49, no. 3, pp. 581–594, Mar. 2014.

[23] M. Schwartz, W. R. Bennett, and S. Stein, "Basic binary communications techniques," in *Communication Systems and Techniques*. IEEE, 1996, pp. 278–313, doi: 10.1109/9780470565292.ch7.

[24] S. Dubouloz, B. Denis, S. de Rivaz, and L. Ouvry, "Performance analysis of LDR UWB non-coherent receivers in multipath environments," in *Proc. IEEE Int. Conf. Ultra-Wideband*, Sep. 2005, pp. 491–496.

[25] N. M. Pletcher, S. Gambini, and J. Rabaey, "A 52 μW wake-up receiver with -72 dBm sensitivity using an uncertain-IF architecture," *IEEE J. Solid-State Circuits*, vol. 44, no. 1, pp. 269–280, Jan. 2009.

[26] X. Chen, Y. Shen, Z. Wang, W. Rhee, and Z. Wang, "A 17 mW 3-to-5 GHz duty-cycled vital sign detection radar transceiver with frequency hopping and time-domain oversampling," *IEEE Trans. Circuits Syst. I, Reg. Papers*, vol. 64, no. 4, pp. 969–980, Apr. 2017.

[27] S. Y. Kim, D.-W. Kang, K.-J. Koh, and G. M. Rebeiz, "An improved wideband all-pass I/Q network for millimeter-wave phase shifters," *IEEE Trans. Microw. Theory Techn.*, vol. 60, no. 11, pp. 3431–3439, Nov. 2012.

[28] B. Wicht, T. Nirschl, and D. Schmitt-Landsiedel, "Yield and speed optimization of a latch-type voltage sense amplifier," *IEEE J. Solid-State Circuits*, vol. 39, no. 7, pp. 1148–1158, Jul. 2004.

[29] D. Vogrig, A. Bevilacqua, A. Gerosa, and A. Neviani, "A symbol-duty-cycled 440-pJ/b impulse radio receiver with 0.57-aJ sensitivity in 130-nm CMOS," *IEEE Trans. Microw. Theory Techn.*, vol. 65, no. 2, pp. 565–573, Feb. 2017.

Bowen Wang (Graduate Student Member, IEEE) received the B.S. degree in integrated circuit design and integrated systems from Xidian University, Xi'an, China, in 2018. He is currently pursuing the Ph.D. degree with the School of Integrated Circuits, Tsinghua University, Beijing, China.

His research interests include mixed-signal and RF circuit design for low-power short-range communications.

Woogeun Rhee (Fellow, IEEE) received the B.S. degree in electronics engineering from Seoul National University, Seoul, South Korea, in 1991, the M.S. degree in electrical engineering from the University of California, Los Angeles, Los Angeles, CA, USA, in 1993, and the Ph.D. degree in electrical and computer engineering from the University of Illinois, Urbana-Champaign, Urbana-Champaign, IL, USA, in 2001.

From 1997 to 2001, he was a Principal Engineer with Conexant Systems, Newport Beach, CA, where he developed low-power, low-cost fractional-N synthesizers. From 2001 to 2006, he was with IBM Thomas J. Watson Research Center, Yorktown Heights, NY, USA, where he worked on clocking area for high-speed I/O serial links. He is currently a Professor with the School of Integrated Circuits, Tsinghua University, Beijing, China. From August 2022 to February 2023, he was a Visiting Professor with Seoul National University. His research interests include energy-efficient short-range radios for mobile IoT, UWB transceivers for secure wireless connectivity, and mixed-signal circuits including phase-locked loops. He has published over 180 IEEE papers and holds 24 U.S. patents.

Dr. Rhee is a Region 10 Ex-Officio AdCom Member of the IEEE SOLID-STATE CIRCUITS SOCIETY (since 2020), an IEEE SOLID-STATE CIRCUITS SOCIETY Chapters Steering Committee Member (since 2021), an IEEE CASS BoG Member as SOLID-STATE CIRCUITS SOCIETY Representative (since 2023), and an IEEE Distinguished Lecturer (2016–2017). He currently serves as an Associate Editor for IEEE OPEN JOURNAL OF THE SOLID-STATE CIRCUIT SOCIETY. He has been an Associate Editor of IEEE JOURNAL OF SOLID-STATE CIRCUITS(2012–2018) and IEEE TRANSACTIONS ON CIRCUITS AND SYSTEMS—II: EXPRESS BRIEFS (2008–2009) and a Guest Editor for IEEE JOURNAL OF SOLID-STATE CIRCUITS Special Issue in November 2012, November 2013, and October 2022. He has served on the Technical Program Committee for several IEEE conferences, including International Conference on Solid-State Circuits,Custom Integrated Circuits Conference, and Asian Solid-State Circuits Conference. He was the TPC Chair of Asian Solid-State Circuits Conference 2021 and currently serves on the Steering Committee for Asian Solid-State Circuits Conference.

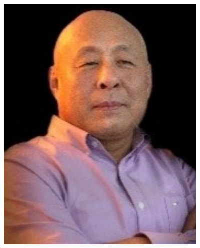

Zhihua Wang (Fellow, IEEE) received the B.S., M.S., and Ph.D. degrees in electronic engineering from Tsinghua University, Beijing, China, in 1983, 1985, and 1990, respectively.

Since 1997 and 2000, he has been a Full Professor and the Deputy Director of the Institute of Microelectronics, Tsinghua University, Beijing, respectively. He was a Visiting Scholar with CMU (1992–1993) and KU Leuven (1993–1994), and a Visiting Professor with HKUST (2014.9–2015.3). His research mainly focuses on CMOS RFIC and biomedical applications, involving RFID, PLL, low-power wireless transceivers, and smart clinic equipment combined with leading-edge RFIC and digital image processing techniques. He has coauthored 13 books/chapters, over 254 (630) papers in international journals (conferences), and over 253 (29) papers in Chinese journals (conferences). He holds 156 Chinese and ten U.S. patents.

Prof. Wang served as the Chairperson for IEEE SOLID-STATE CIRCUITS SOCIETY Beijing Chapter (1999–2009), an AdCom Member for the IEEE SOLID-STATE CIRCUITS SOCIETY (2016–2019), a Technology Program Committee Member for the IEEE International Conference on Solid-State Circuits (2005–2011), a Steering Committee Member for the IEEE Asian Solid-State Circuits Conference (since 2005), the Technical Program Chair for Asian Solid-State Circuits Conference (2013), a Guest Editor for IEEE JOURNAL OF SOLID-STATE CIRCUITS Special Issues (2006.12, 2009.12, and 2014.11), a Distinguished Lecturer for IEEE SOLID-STATE CIRCUITS SOCIETY (2018–2019) and IEEE CASS (2020–2021), an Associate Editor-in-Chief for IEEE OPEN JOURNAL OF CIRCUITS AND SYSTEMS (2019), an Associate Editor for IEEE TRANSACTIONS ON CIRCUITS AND SYSTEMS–I: REGULAR PAPERS, IEEE TRANSACTIONS ON CIRCUITS AND SYSTEMS–II: EXPRESS BRIEFS, and IEEE TRANSACTIONS ON BIOMEDICAL CIRCUITS AND SYSTEMS, and other administrative/expert committee positions in China's national science and technology projects.